PHYSICAL REVIEW FLUIDS **2**, 043901 (2017)

# Numerical simulation and sensitivity analysis of a low-Reynolds-number flow around a square cylinder controlled using plasma actuators

Yosuke Anzai
*Department of Mechanical Engineering, Keio University, Hiyoshi 3-14-1, Kohoku-ku, Yokohama 223-8522, Japan*

Koji Fukagata[*]
*Department of Mechanical Engineering, Keio University, Hiyoshi 3-14-1, Kohoku-ku, Yokohama 223-8522, Japan*

Philippe Meliga
*Aix-Marseille Université, CNRS, Ecole Centrale Marseille, Laboratoire M2P2, Marseille, France*

Edouard Boujo
*LFMI École Polytechnique Fédérale de Lausanne, CH1015 Lausanne, Switzerland and CAPS, ETH Zurich, CH8092 Zurich, Switzerland*

François Gallaire
*LFMI École Polytechnique Fédérale de Lausanne, CH1015 Lausanne, Switzerland*
(Received 17 November 2016; published 25 April 2017)

Flow around a square cylinder controlled using plasma actuators (PAs) is numerically investigated by direct numerical simulation in order to clarify the most effective location of actuator installation and to elucidate the mechanism of control effect. The Reynolds number based on the cylinder diameter and the free-stream velocity is set to be 100 to study the fundamental effect of PAs on two-dimensional vortex shedding, and three different locations of PAs are considered. The mean drag and the root-mean-square of lift fluctuations are found to be reduced by 51% and 99% in the case where two opposing PAs are aligned vertically on the rear surface. In that case, a jet flow similar to a base jet is generated by the collision of the streaming flows induced by the two opposing PAs, and the vortex shedding is completely suppressed. The simulation results are ultimately revisited in the frame of linear sensitivity analysis, whose computational cost is much lower than that of performing the full simulation. A good agreement is reported for low control amplitudes, which allows further discussion of the linear optimal arrangement for any number of PAs.

DOI: 10.1103/PhysRevFluids.2.043901

## I. INTRODUCTION

Flow separation occurring around a bluff body causes a pressure drop on the rear surface and vortex shedding in the wake, which eventually cause drag increase, acoustic emissions, and structural vibrations. In order to mitigate such detrimental effects, various control methods have been proposed and examined [1]. In particular, active control scenarios assuming surface blowing and suction of flows around a circular cylinder [2–8] and a sphere [9–12] have been extensively studied as fundamental examples of flows around bluff bodies. In these examples, the vortex shedding is suppressed typically by delaying the separation. Another well-studied flow configuration is a flow around a body having a blunt trailing edge, of which separation point is fixed at the trailing edge. In

---

[*] fukagata@mech.keio.ac.jp

this case, use of a distributed forcing that three-dimensionalizes the vortex shedding has been shown to work well for drag reduction [13].

Recently, a dielectric barrier discharge (DBD) plasma actuator (PA) has attracted increasing attention as an active control device due to its merits such as its thin and light structure as well as its fast response [14]. For example, Thomas *et al.* [15] experimentally investigated a flow around a circular cylinder at the Reynolds number of $\mathrm{Re} = U^*D^*/\nu^* = 30\,000$ (where $U^*$, $D^*$, and $\nu^*$ denote the free-stream velocity, the cylinder diameter, and the kinematic viscosity, respectively, and the superscript $*$ denotes dimensional quantities) controlled by two-dimensional forcing using PAs, and succeeded in completely eliminating the vortex shedding. Rizzetta and Visbal [16] performed a large eddy simulation of a similar flow at $\mathrm{Re} = 10\,000$ and clarified the details of flow modification. More recently, Igarashi *et al.* [17] performed a direct numerical simulation (DNS) of a similar flow at $\mathrm{Re} = 1\,000$, and demonstrated that the three-dimensional forcing works better than the two-dimensional forcing for the suppression of lift fluctuations.

In the present study, we consider the flow around a square cylinder as another fundamental example, as the knowledge of unsteady flow around cylinders having such noncircular cross sections remains rather limited, even though many engineering structures have square or near-square cross sections (e.g., beams, fences, and other building construction details). The circular and square cylinders share some similarities, including the onset of two-dimensional vortex shedding at $\mathrm{Re} \simeq 50$, followed by a transition to three-dimensional vortex shedding at $\mathrm{Re} \sim 200$. There are, however, important differences that may affect the efficiency of control strategies insofar as the circular cylinder has free separation points, while the square cylinder has separation points pinned either at the trailing or the leading edges, depending on the Reynolds number.

Regarding the use of classical control techniques, Bruneau *et al.* [18] performed two-dimensional numerical simulation of a flow around a square cylinder having a porous surface at $\mathrm{Re} = 300$, $3\,000$, and $30\,000$ and achieved about 30% reduction in the drag force. Zhou *et al.* [19] numerically investigated the effect a control plate located in front of the cylinder at $\mathrm{Re} = 250$ and found the appropriate height and location of the control plate for drag reduction. As for the active control, blowing and suction from the cylinder wall are considered in most of the numerical [20–22] and experimental [23,24] studies. In particular, Kim *et al.* [20] and Saha and Shrivastava [22] studied the effect of base jet and found that the vortex shedding can be completely suppressed when the jet velocity is comparable to the free-stream velocity. Regarding the use of PAs, Gejima *et al.* [25] have recently conducted a wind-tunnel experiment using PAs to suppress vortex shedding from a pantograph head, whose shape is close to a square cylinder.

To the best of authors' knowledge, there has been no numerical study on the control of flow around a square cylinder assuming the use of PAs. The first objective of the present study is, therefore, to investigate the flow around a square cylinder controlled by PAs by means of flow simulation. In order to investigate the fundamental effect of PAs on two-dimensional vortex shedding, we limit our attention to a very low Reynolds number, i.e., $\mathrm{Re} = 100$, and we examine three different arrangements (i.e., locations) of PAs. The second objective is to examine whether the control effect can be reasonably predicted from a linear sensitivity analysis of the uncontrolled flow [26] and whether such an analysis can serve to quickly map the best PAs location without using trial and error.

The paper is organized as follows. The numerical methods are described in Sec. II. Effects of PAs in three different arrangements are discussed in Sec. III with some detailed results on the case similar to the base jet. Prediction by the linear sensitivity analysis is presented in Sec. IV. Finally, conclusions are drawn in Sec. V. In the Appendix, verification and validation of the present numerical simulation are presented.

## II. NUMERICAL METHODS

### A. Flow simulation

We consider a two-dimensional square cylinder in a uniform air flow. The cylinder diameter and the free-stream velocity are assumed to be $D^* = 10\,\mathrm{mm}$ and $U^*_\infty = 0.15\,\mathrm{m/s}$, respectively. Assuming

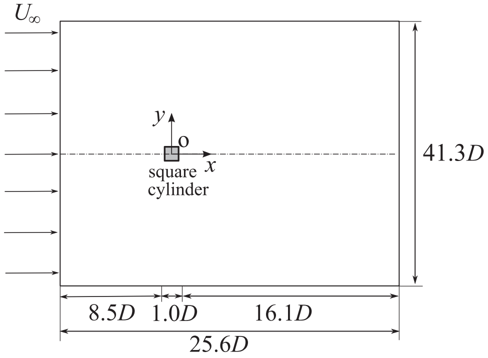

FIG. 1. Flow configuration.

25 °C air at 1 atm, the Reynolds number is $\mathrm{Re} = U_\infty^* D^*/\nu^* = 100$, where $\nu^* = 1.5 \times 10^{-5}$ m$^2$/s is the kinematic viscosity. The flow is assumed to be incompressible and two dimensional.

The governing equations are the continuity equation and the Navier-Stokes equation, i.e.,

$$\frac{\partial u_i}{\partial x_i} = 0, \tag{1}$$

$$\frac{\partial u_i}{\partial t} = -\frac{\partial u_j u_i}{\partial x_j} - \frac{\partial p}{\partial x_i} + \frac{1}{\mathrm{Re}}\frac{\partial^2 u_i}{\partial x_j \partial x_j} + f_i, \tag{2}$$

where $u_i$ and $p$ are the velocity components and the pressure, respectively. All quantities without the superscript $*$ are made dimensionless using $U_\infty^*$, $D^*$, and the fluid density, $\rho^*$. The Einstein summation convention applies to the dummy indices. The last term in Eq. (2), $f_i$, accounts for the body force induced by PAs (detailed in Sec. II B). For notational convenience, $x_1$, $x_2$, $u_1$, and $u_2$ are also denoted by $x$, $y$, $u$, and $v$, respectively.

The flow configuration is shown in Fig. 1. The size of computational domain is $L_x \times L_y = 25.6 \times 41.3$ in $x$ and $y$ directions, respectively, and the distance between the front surface of the square cylinder and the inlet is 8.5. The uniform velocity is imposed at the inflow boundary. At the outflow boundary, the convective velocity condition, i.e.,

$$\frac{\partial u_i}{\partial t} + U_\infty \frac{\partial u_i}{\partial x} = 0, \tag{3}$$

is adopted. At the upper and lower boundaries, the free-slip conditions are imposed:

$$\frac{\partial u}{\partial y} = 0, \quad v = 0, \quad \frac{\partial p}{\partial y} = 0. \tag{4}$$

The no-slip condition is imposed on the cylinder surface using an immersed boundary method of discrete forcing type similar to that of Kim *et al.* [27], although interpolation is not required in the present study since the computational grid is set to always match the cylinder surface.

The present numerical simulation code is based on the DNS code for turbulent channel flow of Fukagata *et al.* [28] extended to a flow with inflow-outflow condition [29]. The equations are spatially discretized using the energy-conservative second-order-accurate finite difference scheme [30,31]. The temporal integration is done using the low-storage, third-order-accurate Runge-Kutta–Crank-Nicolson scheme with velocity-pressure coupling similar to the simplified marker and cell (SMAC) method [32]. The pressure Poisson equation is solved by means of the fast Fourier transform (FFT) in the streamwise ($x$) direction with the mirroring technique [33] and the tridiagonal matrix algorithm (TDMA) in the transverse ($y$) direction.

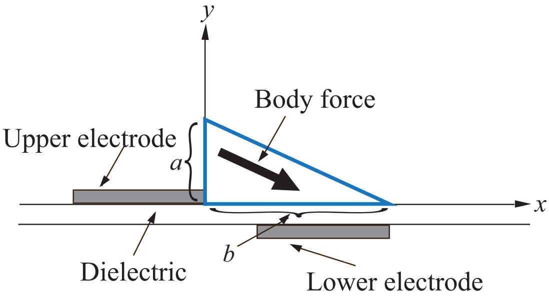

FIG. 2. A schematic of Shyy's model (redrawn based on Shyy *et al.* [35]).

The computational grid is uniform in $x$ direction ($\Delta x = 0.025$). In the $y$ direction, the grid is uniform ($\Delta y = 0.0125$) only in the region near the square cylinder, i.e., $-L_{y,c}/2 \leqslant y \leqslant L_{y,c}/2$, where $L_{y,c}$ denotes the transverse length of the uniform grid region and it is set to be $L_{y,c} = 1.5$. In the outer region, the grid is stretched using geometric series with a growth rate of 1.1. For the choice of these numerical parameters, readers are referred to the validation and verification presented in the Appendix.

### B. Body force by plasma actuator

Strictly speaking, the body force induced by a PA results from very complex unsteady ion-transport phenomena. However, if one is interested in the effect of body force on a relatively low-speed fluid flow, such as the one considered in the present study, it is more efficient to use a time-averaged body force model because the frequency of the imposed AC voltage signal is much higher than that of flow. According to a previous study on the effect of the ratio of these two frequencies on the velocity field [34], a time-averaged body force field can be reasonably used when the typical frequency of flow is less than 30 times of that of the voltage signal. In fact, the vortex shedding frequency under the present flow condition can be estimated as about 2 Hz, and the frequency of the voltage signal is on the order of 10 kHz—hence the aforementioned condition required for the use of time-averaged body force is satisfied.

We use one of the simplest models proposed by Shyy *et al.* [35], as illustrated in Fig. 2. This model assumes a linear decay of the electric field, $E^*(x^*,y^*)$, in a triangular region whose dimensions of sides are $a^*$ and $b^*$, i.e.,

$$E^*(x^*,y^*) = \max(E_0^* - k_1^* x^* - k_2^* y^*, 0), \tag{5}$$

where $E_0^*$ is the maximum electric field strength, and $k_1^*$ and $k_2^*$ are positive constants. We adopt the value of $E_0^*$ proposed by Shyy *et al.* [35], i.e., $E_0^* = 2.2627 \times 10^7$ V/m, while $k_1^* = 4.4782 \times 10^9$ V/m$^2$ and $k_2^* = 8.9564 \times 10^9$ V/m$^2$ are determined so as to be consistent with the dimensions of plasma we assume in the present study, i.e., $a^* = 2.5$ mm and $b^* = 5.0$ mm. Note that $b^* = 5$ mm is a reasonable value concerning the typical plasma progress distance [36]. The electric field vector is assumed to be unidirectional and its components, $E_1^*$ ($x$ component) and $E_2^*$ ($y$ component), are modeled as

$$E_1^* = \frac{k_2^*}{\sqrt{k_1^{*2} + k_2^{*2}}} E^*, \quad E_2^* = -\frac{k_1^*}{\sqrt{k_1^{*2} + k_2^{*2}}} E^*. \tag{6}$$

The time-averaged body force is computed by $f_i^* = \alpha \vartheta^* \delta t^* \rho_c^* e_c^*$, where $e_c^* = 1.60 \times 10^{-19}$ C is the elementary charge; $\vartheta^*$ (the frequency of the applied voltage signal), $\delta t^*$ (the discharge time), and $\rho_c^*$ (the charge number density) are the parameters depending on the operating condition; $\alpha$ (collision

TABLE I. Relationship between the amplitude parameter, $q^*_{\mathrm{eff}}$, and the maximum velocity of the induced flow in a quiescent fluid, $u_{\mathrm{PA}} = u^*_{\mathrm{PA}}/U^*_\infty$, under the flow condition assumed in the study ($D^* = 10$ mm and $U^*_\infty = 0.15$ m/s).

| $q^*_{\mathrm{eff}}$ (C/m$^3$) | $u_{\mathrm{PA}}$ |
|---|---|
| $4.223 \times 10^{-8}$ | 0.01 |
| $8.447 \times 10^{-8}$ | 0.02 |
| $1.689 \times 10^{-7}$ | 0.04 |
| $3.379 \times 10^{-7}$ | 0.1 |
| $6.758 \times 10^{-7}$ | 0.3 |
| $1.352 \times 10^{-6}$ | 0.5 |

frequency) is assumed unity; and $\delta$ is assumed unity if $E^* > E^*_b = 2.09 \times 10^5$ V/m, otherwise zero [35].

By putting these model constants altogether into a single parameter, $q^*_{\mathrm{eff}} = \vartheta^* \delta t^* \alpha \rho^*_c e^*_c$, the effective body force is simply represented as

$$f^*_i = q^*_{\mathrm{eff}} E^*_i. \tag{7}$$

In the flow simulation, this body force is used with the nondimensionalization mentioned above. The amplitude parameter, $q^*_{\mathrm{eff}}$, is adjusted for the desired induced flow velocity according to the relationship between $q^*_{\mathrm{eff}}$ and the maximum induced velocity, $u_{\mathrm{PA}}$, shown in Table I, which was obtained in advance by simulations in a quiescent field.

### C. Locations of plasma actuators

Three different locations of PAs, i.e., cases 1, 2, and 3 shown in Fig. 3, are investigated. Case 1 aims at direct separation delay similarly to the case of circular cylinder. Case 2 is expected to have an effect similar to the base jet. Case 3 is expected to promote the leading edge separation to reduce the trailing edge separation and hasten the reattachment in the wake. As shown in the figure, the four corners of the square cylinder are referred hereafter referred to as A, B, C, and D.

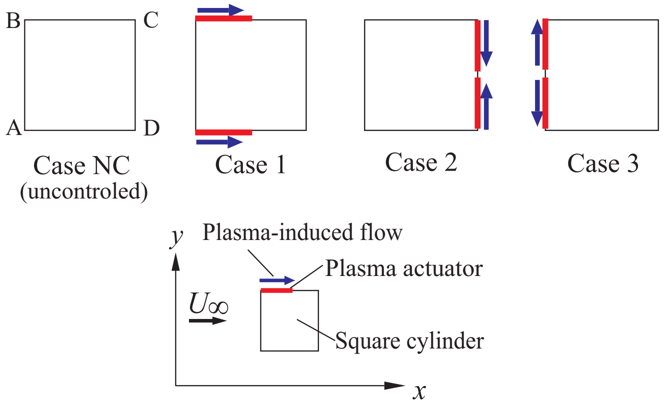

FIG. 3. Arrangements of plasma actuators.

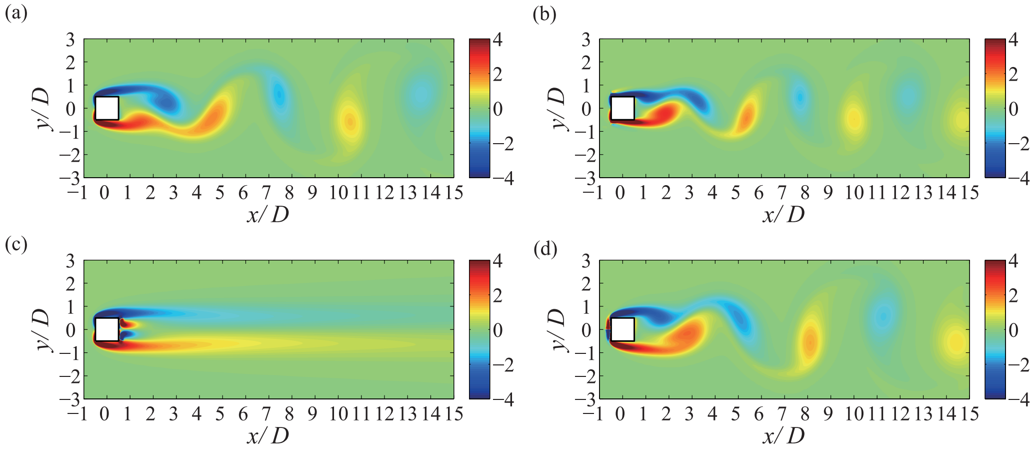

FIG. 4. Instantaneous vorticity distribution: (a) case NC; (b) case 1; (c) case 2; and (d) case 3.

## III. RESULTS AND DISCUSSION

### A. Effects of plasma actuator arrangements

The effects of three different arrangements of PAs are investigated. Similarly to Sec. II, all quantities are made dimensionless using the fluid density, $\rho^*$, the free-stream velocity, $U_\infty^*$, and the cylinder diameter, $D^*$. The maximum induced flow velocity is fixed at $u_{\mathrm{PA}} = 0.5$, and the PAs are operated in the continuous mode (i.e., steady forcing). In the following, the time instant for instantaneous field and the time-averaged statistics are taken after the flow has reached its statistically steady state. The mean quantities are denoted by an overbar $(\bar{\cdot})$ and the root-mean-square (rms) values of the fluctuations are denoted by subscripts $(\cdot_{\mathrm{rms}})$. The integration time for statistics accumulation is 100 dimensionless time, under which the statistical uncertainty is found to be much smaller than the uncertainty due to the grid size presented in the Appendix.

Instantaneous vorticity distributions in the uncontrolled case (case NC) and the controlled cases (cases 1–3) are shown in Fig. 4. As can be clearly seen, the vortex shedding is completely suppressed in case 2, while it remains basically similar in cases 1 and 3, although the width of the vortex street looks slightly decreased in case 1.

Figure 5 shows the time-averaged velocity statistics. In cases NC, 1, and 3, a recirculation region $(\overline{u} < 0)$ is observed right downstream of the square cylinder. The recirculation region is slightly shorter in case 1 than that in cases NC and 3. In case 2, $\overline{u}$ increases near the rear stagnation point and the wake is observed to be significantly elongated as compared to the other cases. The rms streamwise velocity fluctuations, $u_{\mathrm{rms}}$, and the rms transverse velocity fluctuations, $v_{\mathrm{rms}}$, take large values along with the vortex streets; these quantities slightly reduce in case 1 and completely vanish in case 2.

The observations above are quantitatively supported by the mean pressure coefficient, $\overline{C_p}$, and the mean velocity, $\overline{u}/U_\infty$, on the wake centerline $(y = 0)$ as shown in Fig. 6. Here, the pressure coefficient, $C_p$, is defined as

$$C_p = \frac{p - p_\infty}{\frac{1}{2}\rho {U_\infty}^2}, \tag{8}$$

where $p_\infty$ is the free-stream pressure. In case NC, the base pressure (i.e., $\overline{C_p}$ at $x = 0.5$) is negative due to flow separation, which is also obvious from the mean velocity vectors in Fig. 7(a) showing a recirculation region in the wake. As compared to case NC, the base pressure is slightly increased in case 1 and slightly reduced in case 3. The modification observed in case 1 is a typical effect of two-dimensional forcing observed also in the case of circular cylinder [16]. Due to this slight increase

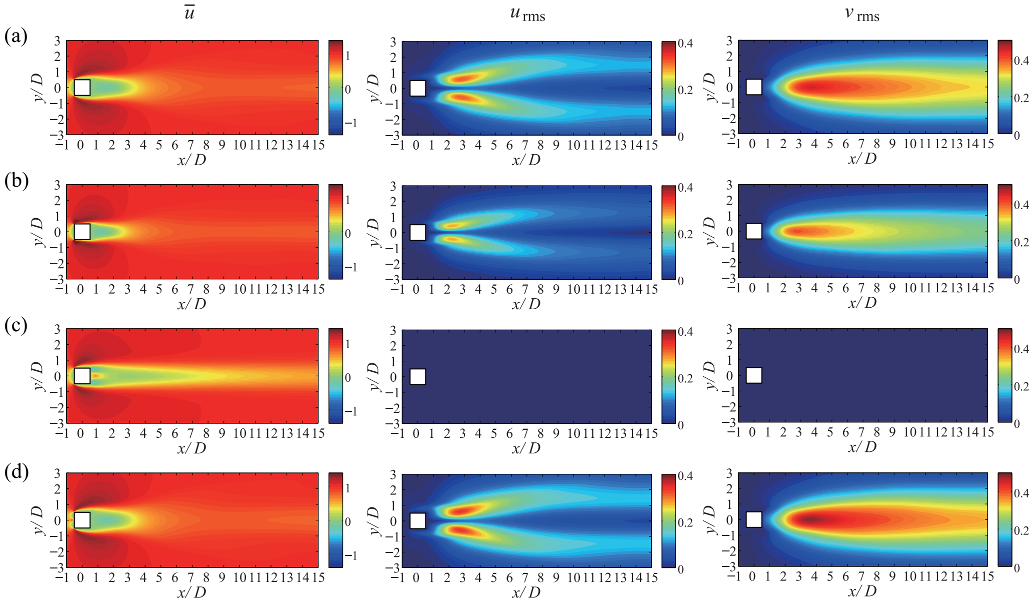

FIG. 5. Time-averaged velocity field: (a) case NC; (b) case 1; (c) case 2; (d) case 3. Left, mean streamwise velocity, $\overline{u}/U_\infty$; middle, rms streamwise velocity fluctuations, $u_{\rm rms}/U_\infty$; right, rms transverse velocity fluctuations, $v_{\rm rms}/U_\infty$.

of the base pressure, the recirculation region is also slightly shortened. In case 2, the base pressure is drastically increased up to $\overline{C_p} \simeq 0$; the minimum pressure is also increased from $\overline{C_p} = -0.8$ in case NC to $\overline{C_p} = -0.4$. As illustrated in Fig. 7(b), this increase of base pressure is due to the impingement of two wall jets induced by two opposing PAs. As a result, a streamwise jet similar to the base jet is produced as initially expected. It is worth noting that the recirculating flows generated near the corners [Fig. 7(b)] and the streamwise variation of the mean centerline velocity [Fig. 6(b)] are also very similar to those observed in the case of base jet [22].

In order to quantitatively investigate the interaction between the upper and lower shear layers, a two-point correlation of velocity fluctuations is computed. The raw two-point correlation function,

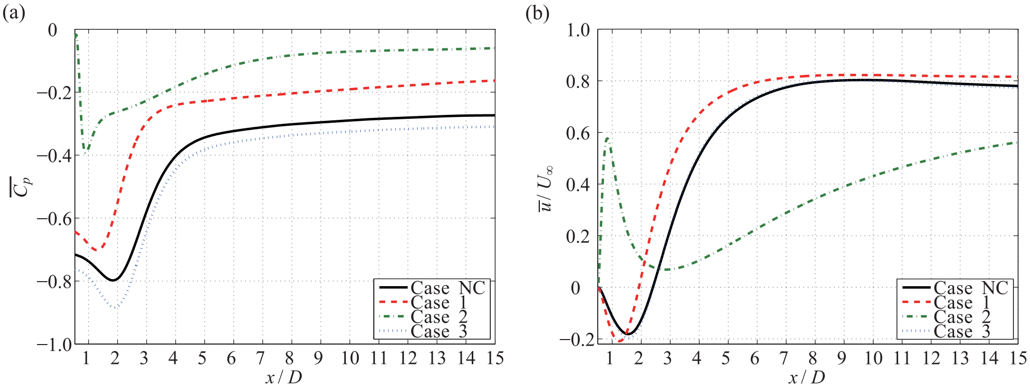

FIG. 6. Statistics on the wake centerline: (a) mean pressure coefficient, $\overline{C_p}$, and (b) mean streamwise velocity, $\overline{u}/U_\infty$.

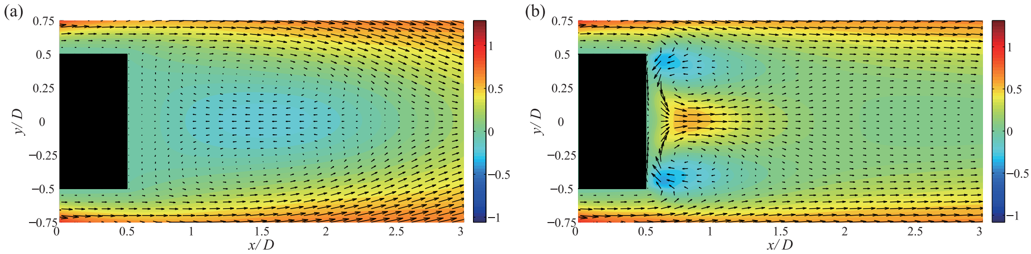

FIG. 7. Mean streamwise velocity (color) and mean velocity vectors near the rear surface: (a) case NC and (b) case 2.

$R_{\mathrm{raw}}$, is defined here as

$$R_{\mathrm{raw}}(x) = \overline{u'_{+}(x,t)u'_{-}(x,t)}. \tag{9}$$

Here, $u'_{+}$ and $u'_{-}$ are the streamwise velocity fluctuations at $y = 0.5$ and $y = -0.5$, respectively, where significant suppression of $u_{\mathrm{rms}}$ was observed, and the overbar denotes time average. Figure 8 shows the raw correlation $R_{\mathrm{raw}}$ and the normalized correlation $R_{\mathrm{norm}} = R_{\mathrm{raw}}/(u_{+,\mathrm{rms}}\, u_{-,\mathrm{rms}})$ in each case, where $u_{+,\mathrm{rms}}$ and $u_{-,\mathrm{rms}}$ denote the rms values of $u'_{+}$ and $u'_{-}$, respectively. In cases NC, 1, and 3, $R_{\mathrm{raw}}$ is negative in the entire region and has the maximum absolute value in the near wake, indicating that the vortex shedding alternately takes place from the upper and the lower surfaces. The maximum absolute value of $R_{\mathrm{raw}}$ is decreased in case 1 and increased in case 3. In case 2, $R_{\mathrm{raw}}$ is nearly zero because the velocity fluctuations are nearly zero. In this case, however, the normalized correlation $R_{\mathrm{norm}}$ indicates that $u'_{+}$ and $u'_{-}$ are nearly perfectly out-of-phase, implying existence of a small amplitude wavy motion.

The force acting on the square cylinder is computed directly using the velocity and pressure field. The pressure and friction forces, $\mathbf{F}_P$ and $\mathbf{F}_F$, are computed as

$$\mathbf{F}_P = \int_S p(-\mathbf{n})dS, \quad \mathbf{F}_F = \int_S \boldsymbol{\tau}\cdot\mathbf{n}dS, \tag{10}$$

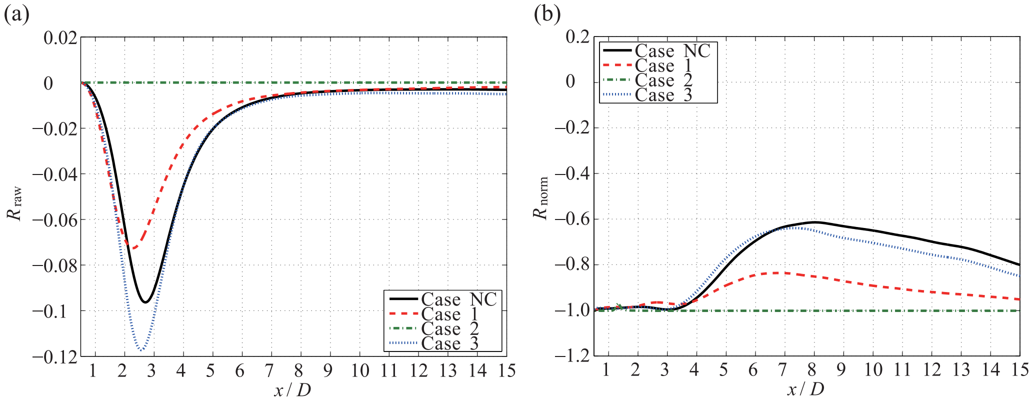

FIG. 8. Two-point velocity correlation of the streamwise velocity fluctuations in the upper and lower shear layers: (*a*) raw correlation $R_{\mathrm{raw}}$ (i.e., the correlation function); (*b*) normalized correlation $R_{\mathrm{norm}}$ (i.e., the correlation coefficient).

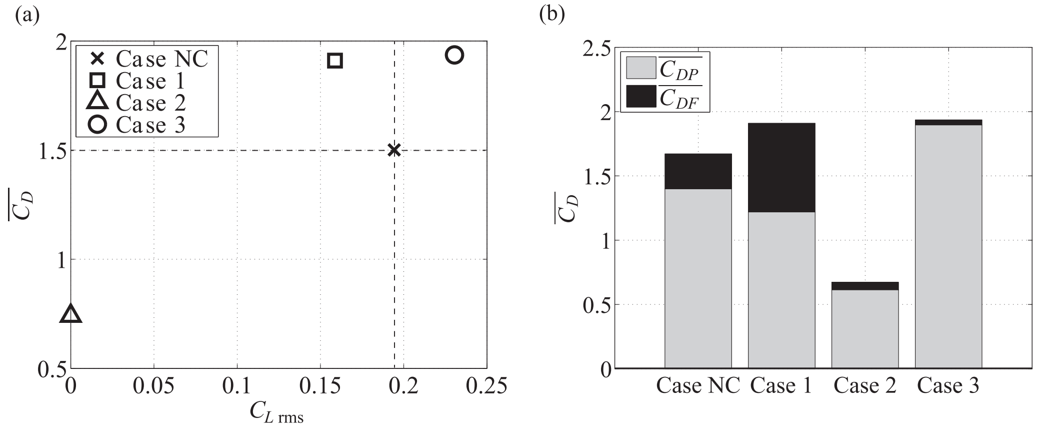

FIG. 9. Mean drag coefficient $\overline{C_D}$ and rms lift coefficient fluctuations $C_{L\,\mathrm{rms}}$: (a) relationship between $C_{L\,\mathrm{rms}}$ and $\overline{C_D}$; (b) decomposition of $\overline{C_D}$ into the friction drag component, $\overline{C_{DF}}$, and the pressure drag component, $\overline{C_{DP}}$.

where $\mathbf{n}$ denotes the unit vector normal to the cylinder surface, $S$, and $\boldsymbol{\tau} = [\nabla \mathbf{u} + (\nabla \mathbf{u})^T]/\mathrm{Re}$ is the viscous stress tensor. The drag and lift coefficients, $C_D$ and $C_L$, are defined as

$$C_D = C_{DP} + C_{DF}, \quad C_L = C_{LP} + C_{LF}, \tag{11}$$

where $C_{DP}$ and $C_{DF}$ are the pressure and friction drag coefficients,

$$C_{DP} = \frac{\mathbf{e}_x \cdot \mathbf{F}_P}{\frac{1}{2}\rho {U_\infty}^2}, \quad C_{DF} = \frac{\mathbf{e}_x \cdot \mathbf{F}_F}{\frac{1}{2}\rho {U_\infty}^2}, \tag{12}$$

and $C_{LP}$ and $C_{LF}$ are the pressure and friction lift coefficients,

$$C_{LP} = \frac{\mathbf{e}_y \cdot \mathbf{F}_P}{\frac{1}{2}\rho {U_\infty}^2}, \quad C_{LF} = \frac{\mathbf{e}_y \cdot \mathbf{F}_F}{\frac{1}{2}\rho {U_\infty}^2}, \tag{13}$$

respectively.

Figure 9(a) shows the relationship between the mean drag coefficient, $\overline{C_D}$, and the rms of lift coefficient fluctuations, $C_{L\,\mathrm{rms}}$. As compared to the uncontrolled case (case NC), the mean drag $\overline{C_D}$ is found to reduce by 51% in case 2, while it increases by 26% and 28% in cases 1 and 3, respectively. The rms of lift fluctuations, $C_{L\,\mathrm{rms}}$, is found to reduce in cases 1 and 2. In particular, the reduction in case 2 amounts to 99% due to the complete suppression of vortex shedding. Figure 9(b) shows the decomposition of $\overline{C_D}$ into the friction drag $\overline{C_{DF}}$ and the pressure drag $\overline{C_{DP}}$. In case 1, $\overline{C_D}$ is increased due to the friction drag, while the pressure drag is decreased. In contrast, the pressure drag is increased in case 3. In case 2, both the pressure drag and the friction drag are reduced. A similar decomposition of $C_{L\,\mathrm{rms}}$ (not shown) indicates that the pressure lift is dominant over the friction lift in all cases and that the change in $C_{L\,\mathrm{rms}}$ is mainly due to the change in the pressure lift.

The changes in the mean drag and the lift fluctuations observed above are explained by the changes in the pressure and the friction coefficients on the cylinder surface. As shown in Fig. 10(a), the mean pressure coefficient, $\overline{C_p}$, is around unity on the front stagnation point (i.e., the midpoint between A and B) and about $-0.7$ on the rear stagnation point (i.e., the midpoint between C and D) in the uncontrolled case (case NC). Due to the collision of flows induced by PAs, the rear stagnation pressure increases in case 2, resulting in the decrease of pressure drag; in contrast, the front stagnation pressure increases in case 3, leading to the increase of pressure drag as observed in Fig. 9(b). Figure 10(b) shows that the pressure fluctuations, $C_{p\,\mathrm{rms}}$, on the upper (B–C) and lower (D–A) surfaces slightly increase in case 3, slightly decrease in case 1, and nearly vanish in

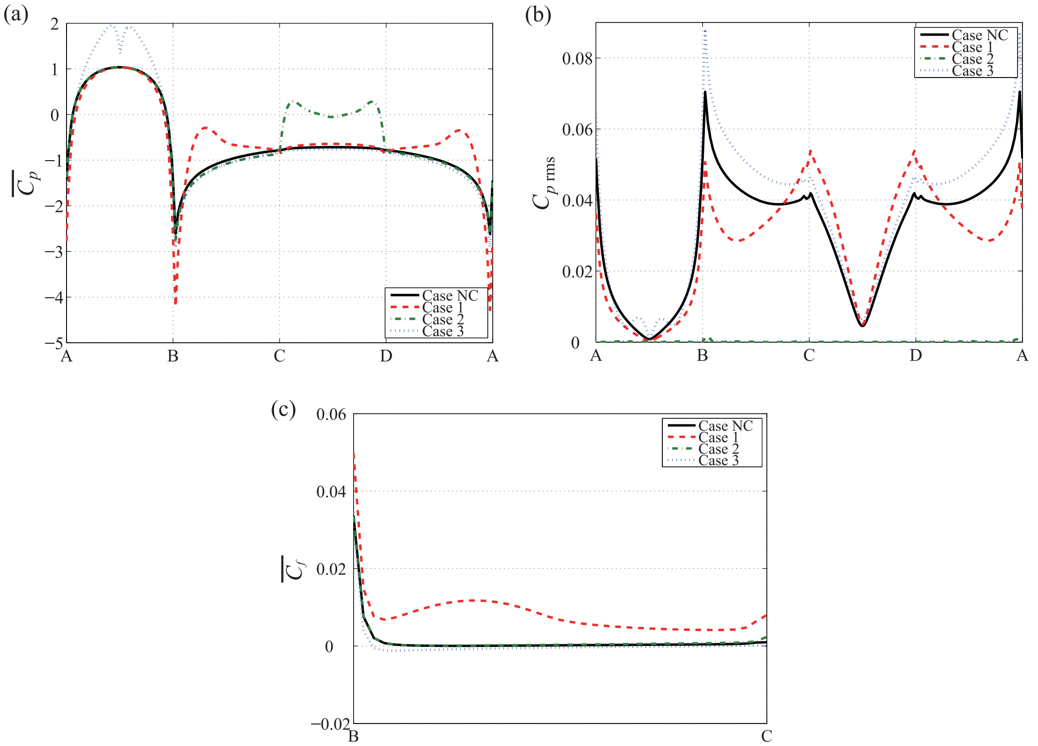

FIG. 10. Pressure and friction coefficients on the cylinder surface: (a) mean pressure coefficient, $\overline{C_p}$; (b) rms of pressure coefficient fluctuations, $C_{p\,\mathrm{rms}}$; and (c) mean friction coefficient, $\overline{C_f}$, on the upper surface.

case 2, leading to the changes observed in Fig. 9(b). Finally, the increase of friction drag in case 1 is explained by the mean friction coefficient $\overline{C_f}$ on the upper surface, defined as

$$\overline{C_f} = \frac{\mathbf{e}_x \cdot \overline{\boldsymbol{\tau}} \cdot \mathbf{n}}{\frac{1}{2}\rho {U_\infty}^2}, \tag{14}$$

As shown in Fig. 10(c), $\overline{C_f}$ significantly increases in case 1 due to the flows induced tangentially to the surface.

### B. Effects of control amplitude in the case of plasma actuators installed on the rear surface

In this subsection, the effect of the control amplitude, $u_{\mathrm{PA}}$, in case 2 (where the PAs installed on the rear surface) is discussed in more details.

Instantaneous vorticity distributions at different control amplitudes are shown in Fig. 11. The vorticity distribution is nearly unchanged up to $u_{\mathrm{PA}} = 0.1$. The starting point of vortex shedding slightly moves downstream at $u_{\mathrm{PA}} = 0.3$; then the vortex shedding is completely suppressed at $u_{\mathrm{PA}} = 0.5$.

The dependence of $C_{L\,\mathrm{rms}}$ and $\overline{C_D}$ on $u_{\mathrm{PA}}/U_\infty$ is presented in Fig. 12. Both $C_{L\,\mathrm{rms}}$ and $\overline{C_D}$ are decreased monotonically as $u_{\mathrm{PA}}/U_\infty$ increases, and the reduction of $C_{L\,\mathrm{rms}}$ takes place faster than that of $\overline{C_D}$. At $u_{\mathrm{PA}}/U_\infty = 0.5$, $C_{L\,\mathrm{rms}}$ decreases by 99% and $\overline{C_D}$ decreases by 51% as stated above.

Figure 13 shows the mean streamwise velocity, $\overline{u}$, on the centerline of the wake. The velocity right downstream of the cylinder increases due to the jet flow induced by PAs as observed above. The clear difference between the vortex shedding case ($u_{\mathrm{PA}} = 0.1$) and the case without vortex shedding ($u_{\mathrm{PA}} = 0.5$) is the presence of a recirculation region. At $u_{\mathrm{PA}} = 0.5$, the induced jet flow is so strong that the region of negative velocity disappears. The maximum jet velocity in this case is

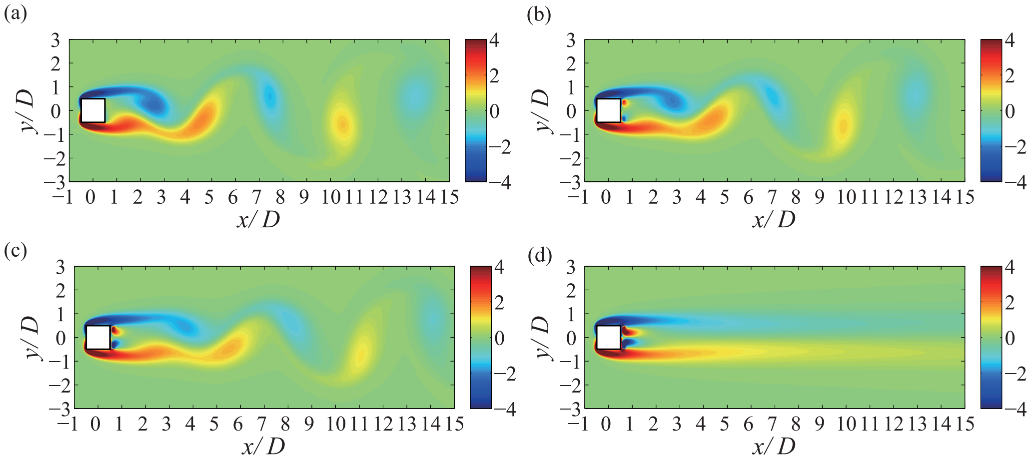

FIG. 11. Instantaneous vorticity distribution in case 2 at different control amplitudes: (a) $u_{\mathrm{PA}}/U_\infty = 0$ (i.e., case NC); (b) $u_{\mathrm{PA}}/U_\infty = 0.1$; (c) $u_{\mathrm{PA}}/U_\infty = 0.3$; (*d*) $u_{\mathrm{PA}}/U_\infty = 0.5$.

about $\overline{u} = 0.6$, which is exactly the same as the blowing velocity required for complete suppression of vortex shedding in the case of base jet [22].

Finally, Fig. 14 shows $\overline{C_p}$ and $C_{p\,\mathrm{rms}}$ on the cylinder surfaces under different control amplitudes. The base pressure increases as $u_{\mathrm{PA}}$ increases while the pressure on other surfaces is nearly unchanged. Thus, it is confirmed that the reduction of $\overline{C_D}$ in case 2 is almost solely due to the streamwise jet induced by the opposing PAs. In contrast, $C_{p\,\mathrm{rms}}$ decreases on all surfaces. Even at $u_{\mathrm{PA}} = 0.1$, the reduction of $C_{p\,\mathrm{rms}}$ is about 70%, which is much larger than the change in the base pressure. This difference explains why the lift fluctuations are suppressed faster than the mean drag as observed in Fig. 12.

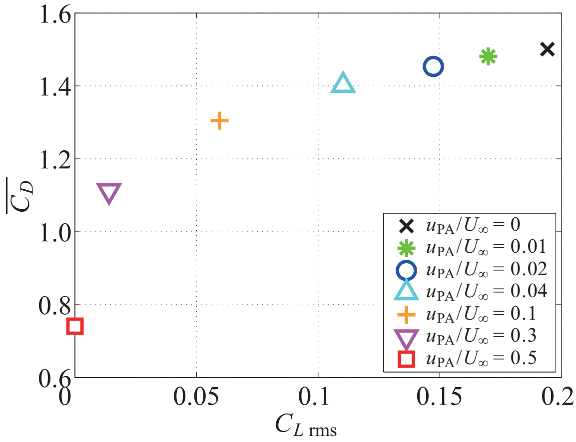

FIG. 12. Relationship between the RMS lift fluctuations, $C_{L\,\mathrm{rms}}$, and the mean drag, $\overline{C_D}$, in case 2 at different control amplitudes.

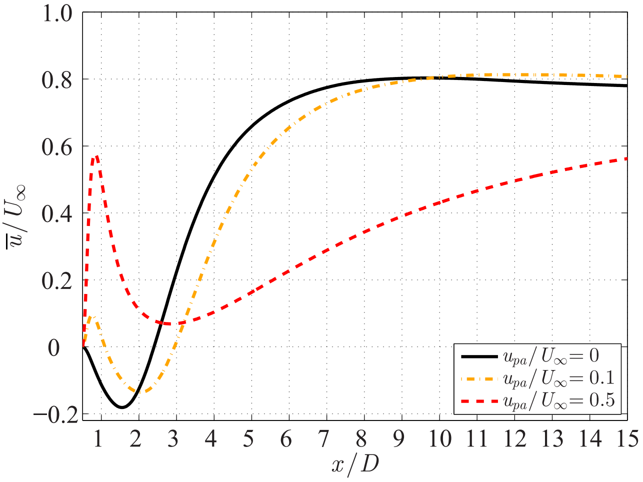

FIG. 13. Mean streamwise velocity, $\overline{u}/U_\infty$, on $y/D = 0$.

## IV. INTERPRETATION IN TERMS OF SENSITIVITY AND LINEAR OPTIMAL PLASMA SETUP

In this section, we look afresh at the obtained results using the framework of linear sensitivity analysis. In the limit of small control amplitudes, the drag and lift variations extracted from the DNS can indeed be expressed as the inner product between the plasma force and sensitivity functions representing the variational derivative of the aerodynamic forces to sources of momentum in the flow (which amounts to invoking the first-order Taylor expansion around zero of $\overline{C_D}$ and $C_{L\,\mathrm{rms}}$ viewed as functions of the plasma force). Such sensitivity frameworks are meant to assess, within one single calculation, the effect of a given control body force (here the plasma force) upon the aerodynamic efforts without having to perform the DNS of the actual controlled state. Unlike bottleneck trial-and-error procedures requiring systematical numerical simulations to be performed over large ranges of parameter spaces, they allow exhaustive coverage of large parameter spaces at very low computational costs, and can therefore serve to map quickly the best arrangements and positions for placement of the PAs, as discussed in the following.

As an inner product, we use here the average over time of the $L_2$ spatial inner product over the computational domain, given that the sensitivity depends on the choice of the inner product structure,

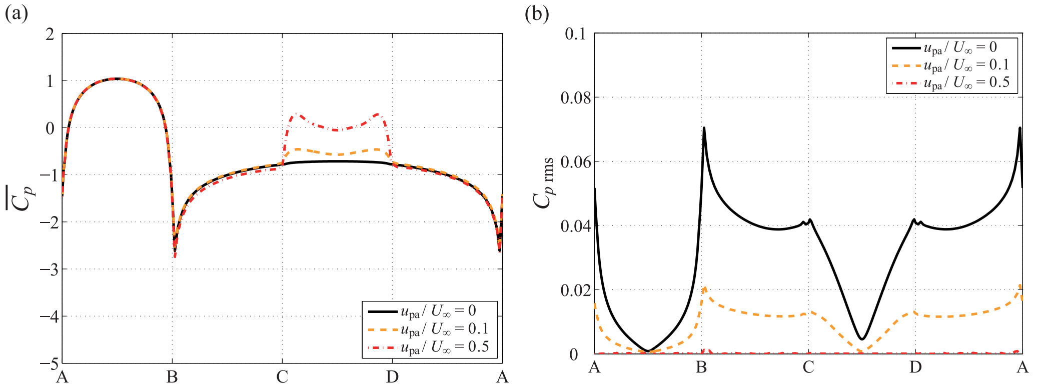

FIG. 14. Pressure distribution on the cylinder surface in case 2 at different control amplitudes: (a) mean pressure coefficient, $\overline{C_p}$; (b) RMS of pressure coefficient fluctuations, $C_{p\,\mathrm{rms}}$.

but that the variation computed from the inner product does not. Using a variational technique based on the computation of Lagrange multipliers, Meliga *et al.* [26] have shown recently that the change in the mean drag induced by the plasma force can be expressed in the limit of infinitesimal control amplitude as

$$\delta\overline{C_D} = \frac{1}{\tau}\int_0^{\tau}\int_S u_i^{\dagger} f_i \, dSdt, \tag{15}$$

where $\tau$ is an averaging time span assumed appropriately large enough to achieve convergence to statistical equilibrium and $u_i^{\dagger}$ and $p^{\dagger}$ denote adjoint velocities and pressure. The solution to the time-dependent equations

$$\frac{\partial u_i^{\dagger}}{\partial x_i} = 0\,, \tag{16}$$

$$-\frac{\partial u_i^{\dagger}}{\partial t} - \frac{\partial u_i^{\dagger}}{\partial x_j}u_j + \frac{\partial u_j^{\dagger}}{\partial x_i}u_j - \frac{\partial p^{\dagger}}{\partial x_i} - \frac{1}{Re_D}\frac{\partial^2 u_i^{\dagger}}{\partial x_j \partial x_j} = 0, \tag{17}$$

with boundary condition at the bluff body surface

$$u^{\dagger} = 2\,, \quad v^{\dagger} = 0, \tag{18}$$

is meant to nullify the boundary term,

$$\frac{1}{\tau}\int_0^{\tau}\int_S \delta\sigma_{ij} n_j (2\delta_{1i} - u_i^{\dagger}) dSdt, \tag{19}$$

that shows up during the derivation of the adjoint equations by integration by parts, where $\delta\sigma_{ij}$ denotes the control-induced perturbation of the stress tensor (that needs not be known explicitly). The change in the rms lift fluctuations can be expressed similarly as

$$\delta C_{L\,\mathrm{rms}} = \frac{1}{\tau}\int_0^{\tau}\int_S u_i^{\dagger} f_i \, dSdt, \tag{20}$$

where $(\boldsymbol{u}^{\dagger}, p^{\dagger})$ now denotes the solution to the same adjoint equations (16) and (17), but with boundary condition at the bluff body surface

$$u^{\dagger} = 0\,, \quad v^{\dagger} = 2\frac{C_L - \overline{C_L}}{C_{L\,\mathrm{rms}}}. \tag{21}$$

We compute here all sensitivities using the finite-elements solver presented in Meliga *et al.* [26], to which the reader is referred for further details (including specifics about the numerical procedure yielding the computation of the adjoint fields and systematical validation tests assessing their accuracy). Suffice it to say here that time discretization is achieved using the second-order accurate Crank-Nicholson scheme with time step $\Delta t = 5 \times 10^{-2}$, that the computational domain is extended to $L_x \times L_y = 90 \times 50$, and that the distance between the front surface of the square cylinder and the inlet is increased to 29.5 to account for the fact that the non-normality of the Navier-Stokes equations [37] reverses the directionality of advection by the cylinder flow in Eq. (17). To Eqs. (16) and (17), we append classical adjoint open flow conditions on the boundary of the computational domain, that consist of homogeneous conditions at the inflow, symmetric conditions at the transverse boundaries, and an adjoint stress-free condition at the outflow [38]. As explained in Meliga *et al.* [26], the adjoint equations must be solved backwards in time starting from the initial condition $u^{\dagger}(\tau) = v^{\dagger}(\tau) = 0$ because the temporal propagation of information also is being reversed. In practice, this requires knowledge of the entire history of the uncontrolled (NC) cylinder flow solution over the time span of interest, which is achieved here performing a dedicated DNS and storing to disk all time steps over 600 time units. The adjoint equations are solved over the same duration. The first and last 100 time units correspond to transient regimes in the direct and adjoint simulations,

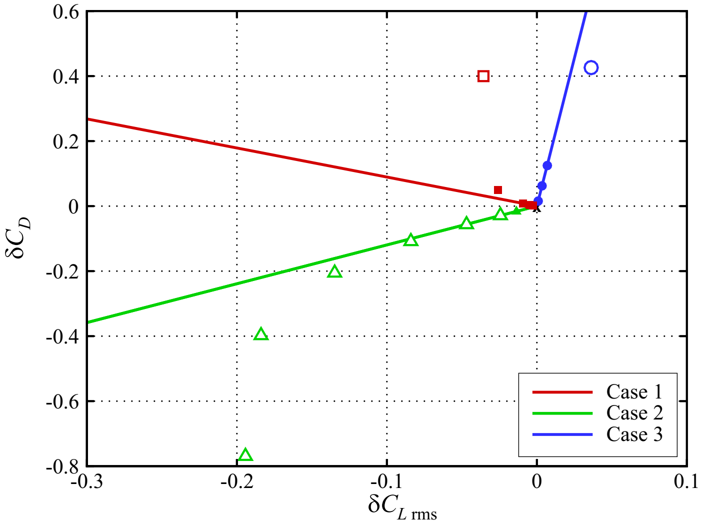

FIG. 15. Effect of the plasma actuator, as assessed from a linear sensitivity analysis. The sensitivity results are indicated by the colored lines. Open symbols denote the finite difference DNS results discussed in Sec. III. Filled symbols denote dedicated finite elements DNS results obtained at low control amplitudes.

respectively, and are discarded when evaluating changes in mean drag [Eq. (15)] and rms lift fluctuations [Eq. (20)].

We show in Fig. 15 the effect of the plasma actuator reported in the $\delta C_{L\ \mathrm{rms}} - \delta\overline{C_D}$ plane. The DNS results obtained with the finite-difference code and documented in the previous sections are reported as the colored open symbols, while sensitivity predictions are shown as the solid lines. For case 2, both sets of results superposed for the smallest control amplitudes, including an additional run at $q^*_{\mathrm{eff}} = 2.112 \times 10^{-8}$ C/m$^3$ ($u_{\mathrm{PA}} \simeq 0.005$) performed with the finite elements solver reported as the smaller filled symbol. This is consistent with the fact that the effect of the control is then linear, yet such an agreement is actually remarkable because the nonlinear and linear results have been obtained using two different codes. The agreement remains satisfying up to moderate control amplitudes of order $q^*_{\mathrm{eff}} = 1.689 \times 10^{-7}$ C/m$^3$ ($u_{\mathrm{PA}} \simeq 0.04$), whereupon nonlinearities come into play. This results in increasing discrepancies, the effect of the control being systematically overestimated by the sensitivity analysis. Note the sensitivity of the mean drag is actually larger than that of the rms lift fluctuations, meaning that the fact that the reduction rate $\delta C_{L\ \mathrm{rms}}$ being larger than that of $\delta\overline{C_D}$ is an artifact of the uncontrolled rms lift fluctuations being smaller. For cases 1 and 3, only large control amplitudes are available from the finite-difference calculations (shown here are the red and blue open symbols), hence the observed dissemblance. Nonetheless, additional, dedicated finite elements DNS performed at small control amplitudes ($q^*_{\mathrm{eff}} = 2.112 \times 10^{-8}$ C/m$^3$ up to $q^*_{\mathrm{eff}} = 8.447 \times 10^{-8}$ C/m$^3$) and reported as the smaller filled symbols in Fig. 15 match perfectly the linear sensitivity predictions. These results provide good evidence that the sensitivity approach carries valuable information in view of guiding efficient control strategy, besides reducing tremendously the numerical effort. Indeed, even though the agreement is only qualitative for large actuation amplitudes, the analysis predicts well the fact that the case 2 arrangement is the only one to reduce both the mean drag and the rms lift fluctuations, while case 1 increases the mean drag and case 3 increases both the mean drag and the rms lift fluctuations.

The analysis can be taken further by using the sensitivity as a systematic guideline on where and how to position the plasma actuators in the attempt to reduce the aerodynamic efforts. Indeed, because the sensitivity framework is linear in essence, the effect of any arrangement of PAs is obtained as the sum of the effects of each individual actuator. For a given number of PAs, this means

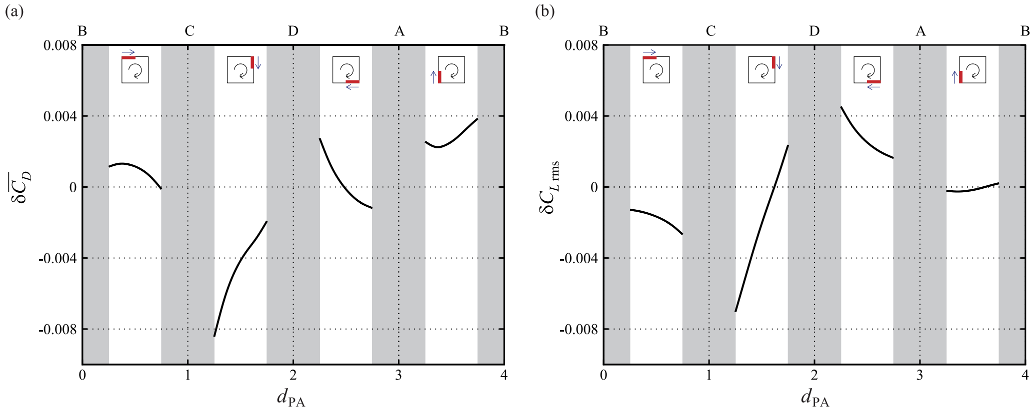

FIG. 16. Effect of one single plasma actuator on the (a) mean drag coefficient and (b) rms of lift coefficient, as assessed from a linear sensitivity analysis. All results reported in terms of the distance $d_{\mathrm{PA}}$ between the (upper-left) corner B and the midpoint of the lower electrode. The gray-shaded areas correspond to regions of the cylinder where no actuator can be placed because the length of the plasma triangular domain exceeds the distance to the nearest edge.

that the (linear) optimal arrangement can be determined easily, provided the effect of one single actuator has been characterized exhaustively, both in terms of position and of orientation with respect to the upstream flow. As an illustration, we show in Fig. 16(a) the change in the mean drag induced by a single PA, taken to be the case 1 upper actuator, initially positioned at the (upper-left) corner B of the square cylinder and translated clockwise along the cylinder surface. Results are reported in terms of the distance $d_{\mathrm{PA}}$ between B and the midpoint of the lower electrode. The gray-shaded areas correspond to regions of the cylinder where no actuator can be placed because the length of the plasma triangular domain exceeds the distance to the nearest edge. The maximum drag reduction is achieved positioning the actuator at $d_{\mathrm{PA}} = 1.25$ (in which case it is virtually identical to the case 2 upper PA), and drag is reduced if the actuator is either anywhere on the base (C–D), or on the lower surface (D–A), close enough to corner A (where it finds itself at the same position as the case 1 lower actuator, but with the plasma induced flow pointing upstream, not downstream). The change in the rms lift fluctuations is reported in Fig. 16(b). It shows that the rms lift fluctuations are now reduced if the actuator is either on the base (C–D) or the upper surface (B–C), close enough to corner C, the maximum reduction being also achieved at $d_{\mathrm{PA}} = 1.25$ for a configuration corresponding to the case 2 upper actuator.

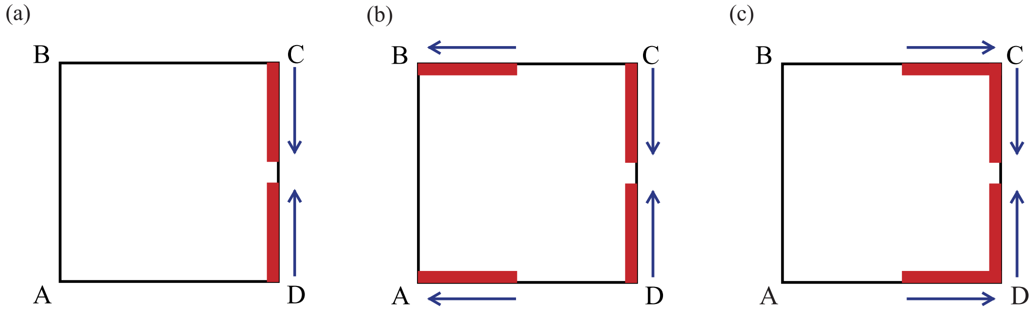

FIG. 17. (a) Optimal arrangement of two PAs in view of reducing the mean drag and the rms lift, as deduced from a linear sensitivity analysis. (b), (c) Optimal arrangement of four PAs in view of reducing the (b) mean drag and (c) rms lift fluctuations.

The change in the mean drag and rms lift fluctuations induced by the symmetric actuator, i.e., the case 1 lower actuator, similarly translated clockwise along the surface from the lower-left edge, is not reported here because the results are identical to those reported in Fig. 16 provided $d_{PA}$ is redefined as the distance between the lower-left edge A and the midpoint of the lower electrode. This is because the shape of the cylinder considered here is symmetric; however, both sets of calculations must be performed in the most general case for the effect of one single actuator to be completely characterized. From these results, we conclude that case 2 is actually the (linear) optimal arrangement of two plasma actuators in view of reducing the mean drag *and* the rms lift fluctuations; see Fig. 17(a). In contrast, for four actuators, the optimal arrangement depends on the target objective: For the mean drag, it is obtained by adding two PAs on the upper and lower surfaces, close to the upstream edges A and B, whose plasma-induced flows point upstream, as illustrated on Fig. 17(b). For the rms lift fluctuations, it is rather obtained placing two PAs close to the downstream edges C and D, whose plasma-induced flows point downstream, as illustrated in Fig. 17(c).

## V. CONCLUSIONS

Flow around a square cylinder controlled using plasma actuators (PAs) is numerically investigated at the Reynolds number based on the cylinder diameter and the freestream velocity of Re = 100.

Investigation on the effects of three different arrangements of PAs reveals that the total drag is not reduced with the classical arrangement, where the actuators are installed on the top and bottom surfaces, due to the increase of friction drag. In contrast, the drag and the lift fluctuations can be reduced simultaneously when the plasma actuators are installed on the rear surface to induce opposing inward flows (case 2). In this case, the pressure differences between the front and rear surfaces are significantly reduced as compared to the uncontrolled case to result in 51% drag reduction. Moreover, the pressure fluctuations vanish due to a complete suppression of vortex shedding to result in 99% reduction in the lift fluctuations. A more detailed investigation in case 2 under different control amplitudes reveals that the jet velocity required to the complete suppression of vortex shedding, i.e., about 50%, is comparable to that in the case using a base jet. Beyond the operating costs (the cost of actuating the PA can actually be higher than that of producing a base jet because a large majority of the electrical energy input dissipates as heat without being converted into kinetic energy), the main advantage of the PA lies in its unique ease of use, as it can be installed on any existing body with little effort.

The simulation results have been successfully compared to theoretical predictions obtained from linear sensitivity analysis to a steady force, used as a valuable tool to assess rapidly the effect of any arrangement of PAs. By doing so, case 2 turns to be the optimal linear arrangement to reduce both the mean drag and the rms lift fluctuations. In contrast, for four actuators, the optimal arrangement depends on the control objective, although it features systematically two actuators at the base and two actuators on the lateral sides. All sensitivity results are obtained beforehand, i.e., without performing the simulations of the controlled states, which suggests that the approach can serve as a relevant tool to predict optimal arrangements of PAs at a low computational cost.

The present numerical simulation and sensitivity analysis were performed assuming that the flow at Re = 100 remains two-dimensional even under the forcing by PAs. This is likely true for the cases where the instability was suppressed (i.e., cases 1 and 2) but not always obvious for the case where the instability was enhanced (i.e., case 3). Investigation on the modification of two-dimensional to three-dimensional transition under various forcing by PAs is therefore left as a future work. In addition, the present study assumed the simplest model to represent the body force induced by PAs. For the design of actual systems, a body force field estimated from the actually measured velocity field [39,40] may alternatively be used because the detailed body force field is highly dependent on various conditions, e.g., ambient humidity, voltage waveform, electrical impedance of the circuit, deterioration of electrodes. As implied by Eqs. (15) and (20), however, the global flow modification should be relatively insensitive to the minute difference in the local body force field if the integrated amount of momentum introduced by PA is the same.

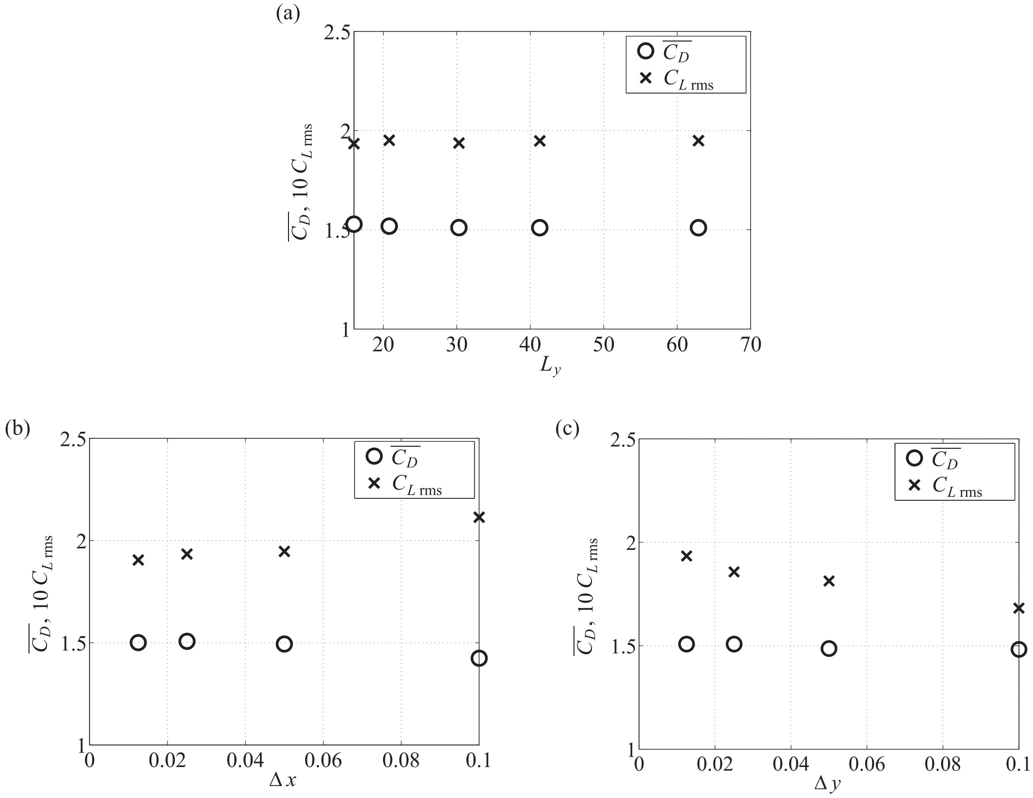

FIG. 18. Dependence of the rms lift fluctuations, $C_{L\,\mathrm{rms}}$, and the mean drag, $\overline{C_D}$, on numerical parameters: (a) dependence on the transverse computational domain size, $L_y$; (b) dependence on the streamwise grid spacing, $\Delta x$; (c) dependence on the transverse grid spacing, $\Delta y$.

## ACKNOWLEDGMENTS

The authors are grateful to Dr. Shinnosuke Obi, Dr. Keita Ando, and Haruhiko Gejima (Keio University) for fruitful discussion. This work was partly supported through a collaborative research program between Keio University and Railway Technical Research Institute (RTRI) (Japan), and Grant-in-Aid for Scientific Research (C) (Grant No. JP25420129) by the Japan Society for the Promotion of Science (JSPS) KAKENHI.

TABLE II. Streamwise grid spacing, $\Delta x$, the transverse grid spacing in the vicinity of the cylinder, $\Delta y$, and the number of grid points, $N_x \times N_y$, used for verification.

| $\Delta x$ | $\Delta y$ | $N_x \times N_y$ |
|---|---|---|
| 0.025 | 0.1 | 1024 × 74 |
| 0.025 | 0.05 | 1024 × 100 |
| 0.025 | 0.025 | 1024 × 134 |
| 0.025 | 0.0125 | 1024 × 190 |
| 0.1 | 0.0125 | 256 × 190 |
| 0.05 | 0.0125 | 512 × 190 |
| 0.025 | 0.0125 | 1024 × 190 |
| 0.0125 | 0.0125 | 2048 × 190 |

TABLE III. Comparison of $\overline{C_D}$ and $C_{L\,\mathrm{rms}}$ obtained using different time steps, $\Delta t$.

| $\Delta t$ | $\overline{C_D}$ | $C_{L\,\mathrm{rms}}$ |
|---|---|---|
| $2.5 \times 10^{-3}$ | 1.5101 | 0.1943 |
| $1.25 \times 10^{-3}$ | 1.5107 | 0.1923 |

## APPENDIX: VERIFICATION AND VALIDATION OF UNCONTROLLED FLOW

The computational domain size has three parameters: the distance from the computational inlet to the cylinder, $L_{x,u}$, the distance from cylinder to the the computational outlet, $L_{x,d}$, and the vertical distance between the upper and the lower boundaries, $L_y$. According to Sohankar *et al.* [41] and Sharma and Eswaran [42], $L_{x,u} = 8.5$ is required to obtained results independent of $L_{x,u}$. In these studies, the downstream distance was taken to be $L_{x,d} = 12.5$ [41] or $L_{x,d} = 16.5$ [42]. Following these studies, we fixed the streamwise domain size to be $L_{x,u} = 8.5$ and $L_{x,d} = 16.1$. In order to determine the vertical size, we performed simulations with different values of $L_y$. As shown in Fig. 18(a), the computed $\overline{C_D}$ and $C_{L\,\mathrm{rms}}$ are relatively insensitive to $L_y$: The maximum differences of $\overline{C_D}$ and $C_{L\,\mathrm{rms}}$ between $L_y = 41.3$ and $L_y = 62.9$ cases are 0.03% and 0.05%. Therefore, $L_y = 41.3$ is used in this study. As a result, the size of computational domain used in the present study is fixed as $L_x \times L_y = 25.6 \times 41.3$, as has been shown in Fig. 1.

Franke *et al.* [43] and Sohankar *et al.* [44] have suggested that the distance from the cylinder surface to the nearest grid point significantly affects $\overline{C_D}$ and $C_{L\,\mathrm{rms}}$. In addition, Sharma and Eswaran [42] have suggested that $C_{L\,\mathrm{rms}}$ has the greatest sensitivity to the grid resolution. Therefore, in this study, four different grid refinements given in Table II are used, and the dependency of the $\overline{C_D}$ and $C_{L\,\mathrm{rms}}$ on the grid resolution is investigated in order to determine the appropriate grid size.

Figure 18(b) shows $C_{L\,\mathrm{rms}}$ and $\overline{C_D}$ computed using different streamwise grid sizes $\Delta x$. As can be found in the figure, $C_{L\,\mathrm{rms}}$ and $\overline{C_D}$ tend to converge with the grid refinement. The differences of $\overline{C_D}$ and $C_{L\,\mathrm{rms}}$ between $\Delta x = 0.025$ and $\Delta x = 0.0125$ cases are 0.44% and 1.5%, respectively.

Figure 18(c) shows $C_{L\,\mathrm{rms}}$ and $\overline{C_D}$ computed using different vertical grid sizes $\Delta y$ in the vicinity of the cylinder. The mean drag coefficient $\overline{C_D}$ tends to converge with the grid refinement. The differences $\overline{C_D}$ between $\Delta y = 0.025$ and $\Delta y = 0.0125$ cases is 0.48%. In contrast, $C_{L\,\mathrm{rms}}$ does not seem to converge likewise. This is likely due to the singularity on the corners, which significantly affect the separation at the leading edge. By extrapolation, however, the uncertainty for $C_{L\,\mathrm{rms}}$ can be estimated to be about 5%.

Based on the information above, $\Delta x = 0.025$ and $\Delta y = 0.0125$ are used in this study, while allowing about 0.5% and 5% of uncertainties in $\overline{C_D}$ and $C_{L\,\mathrm{rms}}$, respectively.

TABLE IV. Comparison of $\overline{C_D}$, $C_{L\,\mathrm{rms}}$, and St at Re = 100.

| Studies | $\overline{C_D}$ | $C_{L\,\mathrm{rms}}$ | St |
|---|---|---|---|
| Present | 1.51 | 0.194 | 0.149 |
| Robichaux *et al.* [45] | 1.53 | | 0.154 |
| Saha [46] | 1.50 | | 0.153 |
| Sahu *et al.* [47] | 1.49 | 0.188 | 0.149 |
| Sen *et al.* [48] | 1.53 | 0.193 | 0.145 |
| Sharma and Eswaran [42] | 1.49 | 0.192 | 0.149 |
| Singh *et al.* [49] | 1.51 | 0.160 | 0.148 |
| Sohankar *et al.* [44] | 1.48 | 0.156 | 0.146 |

Table III shows the values of $\overline{C_D}$ and $C_{L\,\mathrm{rms}}$ obtained with different time steps, $\Delta t = 2.5 \times 10^{-3}$ and $\Delta t = 1.25 \times 10^{-3}$. The differences of $\overline{C_D}$ and $C_{L\,\mathrm{rms}}$ between $\Delta t = 2.5 \times 10^{-3}$ and $\Delta y = 1.25 \times 10^{-3}$ cases are 0.04% and 0.19%. Thus, $\Delta t = 2.5 \times 10^{-3}$ is judged to be small enough not to affect the results.

The validity of the present simulation of the uncontrolled flow around a square cylinder is investigated by comparison with literature. Table IV compares the values of $\overline{C_D}$, $C_{L\,\mathrm{rms}}$, and the Strouhal number of vortex shedding, St, at Re = 100 obtained in the present and previous numerical studies. The maximum differences among all studies are 3.5%, 20%, and 5.2% for $\overline{C_D}$, $C_{L\,\mathrm{rms}}$, respectively. In particular, the present result is in good agreement with the result of Sharma and Eswaran [42], who adopted the similar domain size and grid spacings; the differences between these two results are 1.1%, 1.1%, and 0.3% for $\overline{C_D}$, $C_{L\,\mathrm{rms}}$, and St, respectively.

---

[1] H. Choi, W.-P. Jeon, and J. Kim, Control of flow over a bluff body, Annu. Rev. Fluid Mech. **40**, 113 (2008).
[2] K. Roussopoulos, Feedback control of vortex shedding at low Reynolds numbers, J. Fluid Mech. **248**, 267 (1993).
[3] D. S. Park, D. M. Ladd, and E. W. Hendricks, Feedback control of von Kármán vortex shedding behind a circular cylinder at low Reynolds numbers, Phys. Fluids **6**, 2390 (1994).
[4] C. Min and H. Choi, Suboptimal feedback control of vortex shedding at low Reynolds numbers, J. Fluid Mech. **401**, 123 (1999).
[5] M. Milano and P. Koumoutsakos, A clustering genetic algorithm for cylinder drag optimization, J. Comput. Phys. **175**, 79 (2002).
[6] J. Kim and H. Choi, Distributed forcing of flow over a circular cylinder, Phys. Fluids **17**, 033103 (2005).
[7] H. Naito and K. Fukagata, Control of flow around a circular cylinder for minimizing energy dissipation, Phys. Rev. E **90**, 053008 (2014).
[8] S. J. Illingworth, H. Naito, and K. Fukagata, Active control of vortex shedding: An explanation of the gain window, Phys. Rev. E **90**, 043014 (2014).
[9] O. Ghattas and J.-H. Bark, Optimal control of two- and three-dimensional incompressible Navier-Stokes flows, J. Comput. Phys. **136**, 231 (1997).
[10] P. Bagchi, Flow past a sphere with surface blowing and suction, J. Fluids Eng. **129**, 1547 (2007).
[11] S. Jeon, J. Choi, W.-P. Jeon, H. Choi, and J. Park, Active control of flow over a sphere for drag reduction at a subcritical Reynolds number, J. Fluid Mech. **517**, 113 (2004).
[12] S. Jeon and H. Choi, Suboptimal feedback control of flow over a sphere, Int. J. Heat Fluid Flow **31**, 208 (2010).
[13] J. Kim, S. Hahn, J. Kim, D.-K. Lee, J. Choi, W. P. Jeon, and H. Choi, Active control of turbulent flow over a model vehicle for drag reduction, J. Turbul. **5**, N19 (2004).
[14] T. C. Corke, C. L. Enloe, and S. P. Wilkinson, Dielectric barrier discharge plasma actuators for flow control, Annu. Rev. Fluid Mech. **42**, 505 (2010).
[15] F. O. Thomas, T. C. Corke, M. Iqbal, A. Kozlov, and D. Schatzman, Optimization of dielectric barrier discharge plasma actuators for active aerodynamic flow control, AIAA J. **47**, 2169 (2009).
[16] D. P. Rizzetta and M. R. Visbal, Large eddy simulation of plasma-based control strategies for bluff body flow, AIAA J. **47**, 717 (2009).
[17] T. Igarashi, H. Naito, and K. Fukagata, Direct numerical simulation of flow around a circular cylinder controlled using plasma actuators, Math. Probl. Eng. **2014**, 591807 (2014).
[18] C. Bruneau and I. Mortazavi, Passive control of the flow around a square cylinder using porous media, Int. J. Meth. Fluids **46**, 415 (2004).
[19] L. Zhou, M. Cheng, and K. C. Hung, Suppression of fluid force on a square cylinder by flow control, J. Fluids Struct. **21**, 151 (2005).

[20] D.-H. Kim, K.-S. Yang, and J.-S. Eom, Confined vortex shedding past a square cylinder with a planar Jet, JSME Int. J. Ser. B **46**, 316 (2003).

[21] D. R. Arcas and L. G. Redekopp, Aspects of wake vortex control through base blowing/suction, Phys. Fluids **16**, 452 (2004).

[22] A. K. Saha and A. Shrivastava, Suppression of vortex shedding around a square cylinder using blowing, Sādhanā **40**, 769 (2015).

[23] B. Çuhadaroğlu, Y. E. Akansu, and A. Ö. Turhal, An experimental study on the effects of uniform injection through one perforated surface of a square cylinder on some aerodynamic parameters, Exp. Therm. Fluid Sci. **31**, 909 (2007).

[24] Y. E. Akansu and E. Firhat, Control of flow around a square prism by slot jet injection from the rear surface, Exp. Therm. Fluid Sci. **34**, 906 (2010).

[25] H. Gejima, R. Takinami, K. Fukagata, T. Mitsumoji, T. Sueki, and M. Ikeda, Suppression of vortex shedding from a pantograph head using vortex generator-type plasma actuators, J. Fluid Sci. Technol. **10**, JFST0006 (2015).

[26] P. Meliga, E. Boujo, G. Pujals, and F. Gallaire, Sensitivity of aerodynamic forces in laminar and turbulent flow past a square cylinder, Phys. Fluids **26**, 104101 (2014).

[27] J. Kim, D. Kim, and H. Choi, An immersed-boundary finite-volume method for simulations of flow in complex geometries, J. Comput. Phys. **171**, 132 (2001).

[28] K. Fukagata, N. Kasagi, and P. Koumoutsakos, A theoretical prediction of friction drag reduction in turbulent flow by superhydrophobic surfaces, Phys. Fluids **18**, 051703 (2006).

[29] Y. Kametani and K. Fukagata, Direct numerical simulation of spatially developing turbulent boundary layer with uniform blowing or suction, J. Fluid Mech. **681**, 154 (2011).

[30] T. Kajishima, Finite-difference method for convective terms using non-uniform grid, Trans. JSME/B **65**, 1607 (1999).

[31] F. E. Ham, F. S. Lien, and A. B. Strong, A fully conservative second-order finite difference scheme for incompressible flow on nonuniform grids, J. Comput. Phys. **177**, 117 (2002).

[32] A. A. Amsden and F. H. Harlow, A simplified MAC technique for incompressible fluid flow calculations, J. Comput. Phys. **6**, 322 (1970).

[33] A. Mitsuishi, K. Fukagata, and N. Kasagi, Near-field development of large-scale vortical structures in a controlled confined coaxial jet, J. Turbul. **8**, N23 (2007).

[34] S. Yamamoto and K. Fukagata, Numerical simulation of a plasma actuator based on ion transport, J. Appl. Phys. **113**, 243302 (2013).

[35] W. Shyy, B. Jayaraman, and A. Andersson, Modeling of glow discharge-induced fluid dynamics, J. Appl. Phys. **92**, 6434 (2002).

[36] J. R. Roth and X. Dai, Optimization of the aerodynamic plasma actuator as an electrohydrodynamic electrical device, in *Proceedings of 44th AIAA Aerospace Sciences Meeting and Exhibit, 9-12 January 2006, Reno, Nevada*, AIAA Paper 2006-1203 (AIAA, Reston, VA, 2006).

[37] J.-M. Chomaz, Global instabilities in spatially developing flows: Non-normality and nonlinearity, Annu. Rev. Fluid Mech. **37**, 357 (2005).

[38] O. Marquet, D. Sipp, and L. Jacquin, Sensitivity analysis and passive control of cylinder flow, J. Fluid Mech. **615**, 221 (2008).

[39] M. Kotsonis, S. Ghaemi, L. Veldhuis, and F. Scarano, Measurement of the body force field of plasma actuators, J. Phys. D **44**, 045204 (2011).

[40] K. Ota, T. Sekiya, and H. Nishida, Effects of flow measurement resolution on quasi-steady body force estimation in dielectric-barrier-discharge plasma actuator, AIP Adv. **6**, 105109 (2016).

[41] A. Sohankar, C. Norberg, and L. Davidson, Simulation of three-dimensional flow around a square cylinder at moderate Reynolds numbers, Phys. Fluids **11**, 288 (1999).

[42] A. Sharma and V. Eswaran, Heat and fluid flow across a square cylinder in the two-dimensional laminar flow regime, Numer. Heat Transfer A **11**, 247 (2004).

[43] R. Franke, W. Rodi, and B. Schönung, Numerical calculation of laminar vortex-shedding flow past cylinders, J. Wind Eng. Ind. Aerodyn. **35**, 237 (1990).

[44] A. Sohankar, C. Norberg, and L. Davidson, Low-Reynolds number flow around a square cylinder at

incidence: Study of blockage, onset of vortex shedding, and outlet boundary condition, Int. J. Numer. Meth. Fluids **26**, 39 (1998).

[45] J. Robichaux, S. Balachandar, and S. P. Vanka, Three-dimensional Floquet instability of the wake of square cylinder, Phys. Fluids **11**, 560 (1999).

[46] A. Saha, Effect of transitions on flow past a square cylinder at low Reynolds number, J. Eng. Mech. **135**, 839 (2009).

[47] A. K. Sahu, R. P. Chhabra, and V. Eswaran, Two-dimensional unsteady laminar flow of a power law fluid across a square cylinder, J. Non-Newtonian Fluid Mech. **160**, 157 (2009).

[48] S. Sen, S. Mittal, and G. Biswas, Flow past a square cylinder at low Reynolds numbers, Int. J. Numer. Meth. Fluids **67**, 1160 (2011).

[49] A. P. Singh, A. K. De, V. K. Carpenter, V. Eswaran, and K. Muralidhar, Flow past a transversely oscillating square cylinder in free stream at low Reynolds numbers, Int. J. Numer. Meth. Fluids **61**, 658 (2009).